Hindawi Publishing Corporation
Mathematical Problems in Engineering
Volume 2013, Article ID 429094, 13 pages
http://dx.doi.org/10.1155/2013/429094

Research Article

Micro Surface Defect Detection Method for Silicon Steel Strip Based on Saliency Convex Active Contour Model

Kechen Song and Yunhui Yan

School of Mechanical Engineering & Automation, Northeastern University, Shenyang, Liaoning 110819, China

Correspondence should be addressed to Kechen Song; unkechen@gmail.com

Received 20 September 2013; Accepted 22 November 2013

Academic Editor: Gianluca Ranzi

Accurate detection of surface defect is an indispensable section in steel surface inspection system. In order to detect the micro surface defect of silicon steel strip, a new detection method based on saliency convex active contour model is proposed. In the proposed method, visual saliency extraction is employed to suppress the clutter background for the purpose of highlighting the potential objects. The extracted saliency map is then exploited as a feature, which is fused into a convex energy minimization function of local-based active contour. Meanwhile, a numerical minimization algorithm is introduced to separate the micro surface defects from cluttered background. Experimental results demonstrate that the proposed method presents good performance for detecting micro surface defects including spot-defect and steel-pit-defect. Even in the cluttered background, the proposed method detects almost all of the microdefects without any false objects.

1. Introduction

Silicon steel strip is a soft magnetic material that is mainly used as core material in transformers and dynamos. The surface quality of silicon steel strip directly affects the quality and magnetic properties of the final product. Therefore, accurate detection of surface defect has become an indispensable section in steel industry. In recent years, the visual-based inspection technology, as a kind of noncontact inspection method, has become a research hotspot in the field of surface defect inspection. In view of the characteristics of the real time and easines to realize intelligently, this technology has been widely used in online real-time inspection of automatic production lines [1–3].

In order to detect the surface defects automatically, a wide variety of methods have been developed in many applications. Caleb-Solly and Smith [4] described a reconfigurable surface inspection system, which involves using evolutionary algorithms to enable the user to interactively search the local space of image processing parameters and to evolve an optimum set based on the user's visual evaluation. Li et al. [5] proposed a feature-preserving "snake-projection" method to detect the defect seam. In addition, Pan et al. [6] exploited an engineering-driven rule-based detection (ERD) method for bleed detection in visual images which lie in the low signal-to-noise ratio. Yun et al. [7] divided defects into two classes and, respectively, employed undecimated wavelet transform and statistical approach to detect defects. Meanwhile, Yun et al. [8] developed the univariate dynamic encoding algorithm for searches (uDEAS) to detect the cracks. Besides, Bulnes et al. [9] introduced the clustering method to detect periodical defects. Landström and Thurley [10] focused on automated detection of longitudinal cracks in steel slabs based on morphology theory. Recently, Zhang et al. [11] exploited a target identification system based on adaptive genetic algorithm and feature saliency to detect surface defects of copper strip.

Despite the fact that the several methods mentioned above have achieved moderate results in a certain single type of defects, it has not yet become a universal method for all of the surface defects. Therefore, it is necessary to develop an appropriate detection method for micro surface defect of silicon steel strip. Since the surface defects of silicon steel strip are small, it is more difficult to detect

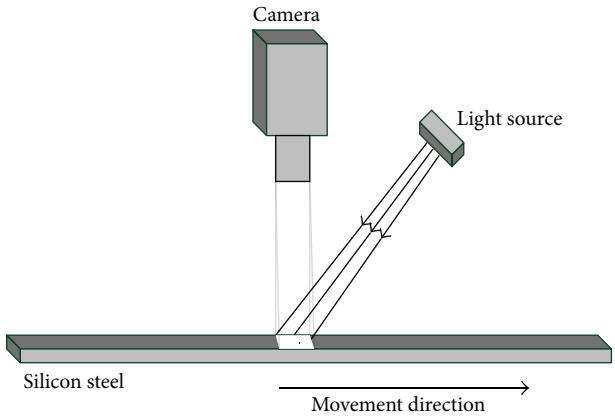

Figure 1: Schematic of the image acquisition.

these microobjects. Furthermore, the cluttered background increases the difficulty of detecting the defects in images.

In recent years, local energy functions based on active contour have been introduced for object detection, which makes it possible to detect micro surface defect of silicon steel strip in images with cluttered background. In this work, a new detection method based on saliency convex active contour model (SCACM) is proposed to detect micro surface defects of silicon steel strip. In the proposed method, visual saliency extraction is employed to suppress the clutter background. The extracted saliency map is exploited as a feature to represent the pixels in the proposed model. Then, the above feature is fused into a convex energy minimization function of local-based active contour. Finally, a fast and accurate numerical minimization algorithm is introduced to separate the micro surface defects from cluttered background.

The rest of this paper is organized as follows. Section 2 presents the hardware configuration of image acquisition and the analysis of micro surface defect. Section 3 introduces the proposed saliency convex active contour model in detail. Then Section 4 elaborates the experiments and discusses the experimental results. Finally, Section 5 concludes the paper.

2. Image Acquisition and Analysis of Micro Surface Defect

The hardware configuration of the image acquisition mainly includes two components: light source and camera. The layout of the acquisition equipment is shown in Figure 1. The light source provides the illumination to make the surface defects visible and helps to capture the surface defect images with camera. Since the light-emitting diode (LED) has many advantages such as little power and longevity, it is used to provide stable illumination. In this work, the LED is made by CCS Incorporated Company of Japan with the model number HLND-1200-SW2. In order to obtain the micro surface defect image, an area scan CCD camera is used. The camera used here is made by Basler of Germany with the model number acA640-90uc. It has a resolution of 658 × 492 pixels with frame rate 90 fps and color image. In this work, the captured color image is resized as 640 × 480 pixels for the purpose of calculating expediently for defect detection. In addition, a 55 mm focal length lens is installed on the camera.

One of the original micro surface defect images of silicon steel strip is shown in Figure 2. As it could be seen in Figure 2(a), the original defect image represents an area of $9.6 \times 7.2\,\text{mm}^2$ in real silicon steel strip. It is observed that the defect image contains two components: the interesting microdefect object and the cluttered background. The former is to be detected while the latter is useless. To illustrate the scale of microdefect object, an area of 60 × 60 pixels is cropped from original defect image. The cropped area represents an area of $0.9 \times 0.9\,\text{mm}^2$ in real silicon steel strip, which is shown in Figure 2(b). Then, the defect area in Figure 2(c) is extracted from the cropped area. From Figure 2(c), we can see that the defect area consists of 6 × 6 pixels; that is, the size of microdefect object is an area of $90 \times 90\,\mu\text{m}^2$ in real silicon steel strip. Obviously, it is quite difficult to detect the microdefect object for most of the current detection methods whose size of defect object is an area of $0.5 \times 0.5\,\text{mm}^2$.

Furthermore, the background of original microdefect image is quite complex, which is another difficult problem for detecting the defect. Despite the fact that the clutter background has certain characters of texture, these characters are more random than regular texture. The surface plot of Figure 2(a) is shown in Figure 3. As it could be seen in Figure 3, the clutter background has random distribution in the whole image.

In addition, due to the surface roughness of silicon steel strip, the microdefect image contains some interference like noise in clutter background. This interference, to some extent, increases the difficulty of detecting the defects in images.

3. Saliency Convex Active Contour Model

In this section, the proposed method is described in two subsections. Firstly, a saliency extraction approach is introduced in Section 3.1 for the purpose of highlighting the potential objects to get a saliency map. Then, the saliency map is fused into a convex energy minimization function in Section 3.2.

3.1. Saliency Extraction. Saliency extraction is an important step in machine vision, which has been applied in many tasks including object detection and image segmentation. An excellent saliency extraction method can well highlight the potential objects to get a saliency map. However, most of the current saliency methods often generate saliency maps that have low resolution or poorly defined borders. Furthermore, some methods may generate maps that have ill-defined object boundaries.

In order to avoid these drawbacks mentioned above, Achanta et al. [12] exploited a frequency-tuned approach to estimate center-surround contrast using color and luminance features. Although the frequency-tuned approach created full resolution saliency maps with well-defined boundaries of salient objects, it may fail to correctly highlight the salient regions in the presence of microsalient objects and complex textured background. In this work, the symmetric surround

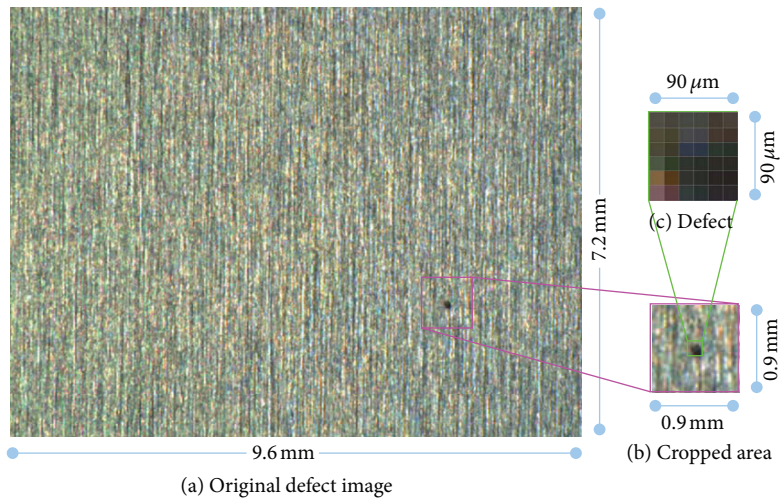

FIGURE 2: Sample image of micro surface defect.

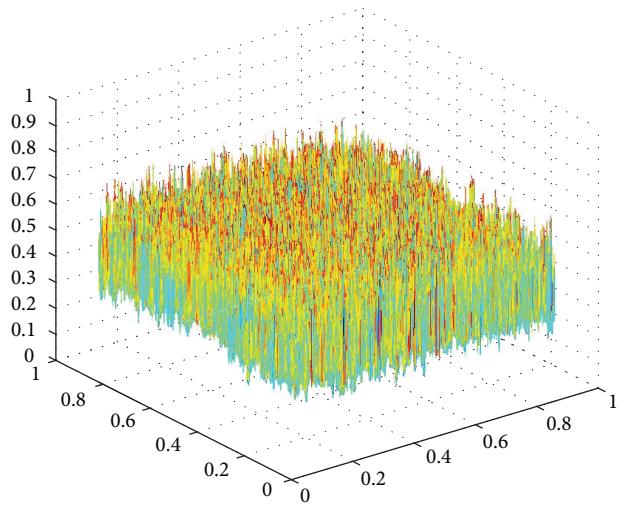

FIGURE 3: Surface plot of the defect sample image in Figure 2.

saliency [13] is employed to improve the frequency-tuned approach.

For an input image $\mathbf{I}$, the symmetric surround saliency value $S(x, y)$ is obtained as

$$S(x, y) = \left\| \mathbf{I}_{\mu}(x, y) - \mathbf{I}_{f}(x, y) \right\|, \tag{1}$$

where $\mathbf{I}_f(x, y)$ is the corresponding image Lab color space vector value in the Gaussian blurred version (using an $\mathbf{N} \times \mathbf{N}$ separable binomial kernel) of the original image and $\| \cdot \|$ is the L_2 norm. Here, the L_2 norm is the Euclidean distance. In the Lab color space, each pixel location is a $[L, a, b]^T$ vector. Different from the mean image feature vector of the frequency-tuned approach [12], $\mathbf{I}_{\mu}(x, y)$ is the average Lab vector of the subimage whose center pixel is at position (x, y) as given by

$$\mathbf{I}_{\mu}(x, y) = \frac{1}{A} \sum_{i=x-x_0}^{x+x_0} \sum_{j=y-y_0}^{y+y_0} \mathbf{I}(i, j) \tag{2}$$

with offsets x_0 and y_0 and area A of the subimage computed as

$$\begin{aligned} x_0 &= \min(x, w - x), \\ y_0 &= \min(y, h - y), \\ A &= (2x_0 + 1)(2y_0 + 1), \end{aligned} \tag{3}$$

where w and h are width and height of an input image, respectively.

To illustrate the calculation procedure of the symmetric surround saliency, Figure 4 presents the schematic of the saliency extraction for input defect image. Firstly, the original defect image (Figure 4(a)) is blurred by $\mathbf{N} \times \mathbf{N}$ Gaussian filter window ($\mathbf{N}$ is set as 5). Then, Lab color space images (i.e., Figures 4(c) and 4(d)) of original image (i.e., Figure 4(a)) and filter image (i.e., Figure 4(b)) are obtained by converting color space from RGB to Lab. Equation (2) is used to compute the Lab average vector $\mathbf{I}_{\mu}(x, y)$. Finally, the symmetric surround saliency value $S(x, y)$ is obtained with (1).

For the input defect image (Figure 4(a)), the obtained saliency map and its surface plot are shown in Figure 5. As it could be seen in Figure 5(a), the saliency map image by saliency extraction is properly able to suppress the textured background and amplify the difference between the interesting defect object and the textured background. Moreover, in the surface plot image which is shown in Figure 5(b), the contrast between defect object and textured background could be obviously recognized as one peak in the image. This surface plot image confirms that the symmetric surround saliency value is better than the intensity value for micro surface defect object in a textured background.

FIGURE 4: Schematic of the saliency extraction for the input defect image.

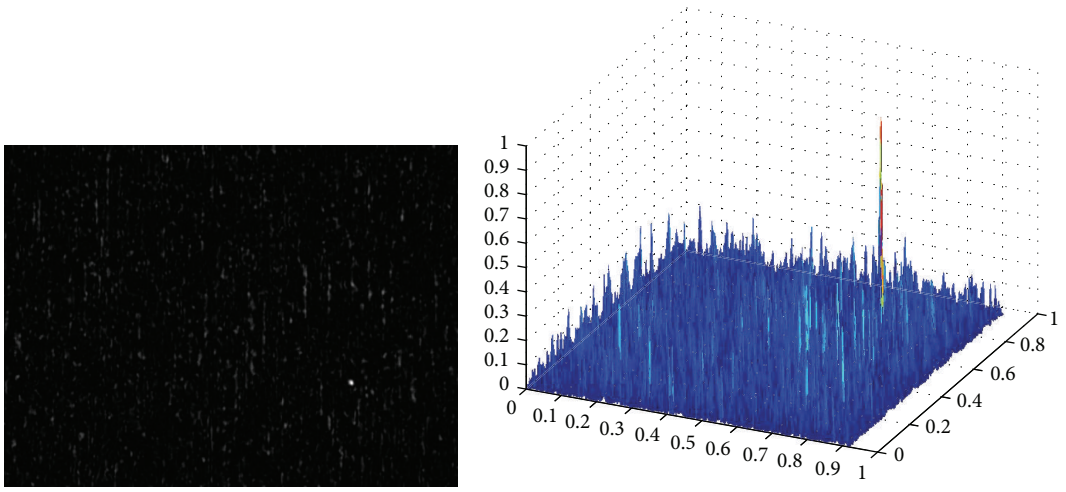

(a) Saliency map (b) Surface plot of saliency map

FIGURE 5: Saliency map and its surface plot.

3.2. Saliency Convex Active Contour Model. The extracted saliency map in Section 3.1 is exploited as a feature to represent the pixels. In view of the statistical information of the above feature, this feature is fused into a convex energy minimization function of local-based active contour; that is, the saliency convex active contour model (SCACM) is proposed.

The energy function of local-based active contour is firstly defined as

$$\begin{aligned} &\min_C E(m_1, m_2, C) \\ &= \int_C L(s, C)\, ds + \lambda \int_{\text{inside}(C)} |S(x) - m_1|^2 dx \\ &\quad + \lambda \int_{\text{outside}(C)} |S(x) - m_2|^2 dx, \end{aligned} \tag{4}$$

where $L(s, C)$ is the function with respect to the length of curve C, s is the integral variable for the length of curve C, λ is a fixed parameter, $S(x)$ is saliency map, and m_1 and m_2 are two constants that approximate the image intensities inside and outside the contour C, respectively:

$$m_1 = \text{mean}\left(S \in \left(\{x \in \Omega \mid \phi(x) < 0\} \cap W_k(x)\right)\right), \tag{5}$$

$$m_2 = \text{mean}\left(S \in \left(\{x \in \Omega \mid \phi(x) > 0\} \cap W_k(x)\right)\right), \tag{6}$$

where $W_k(x)$ is a local Gaussian window with standard deviation σ, and size of the window is determined as $(4\sigma + 1) \times (4\sigma + 1)$.

Equation (4) is usually handled with the level set method (LSM), where C is represented by a level set function ϕ.

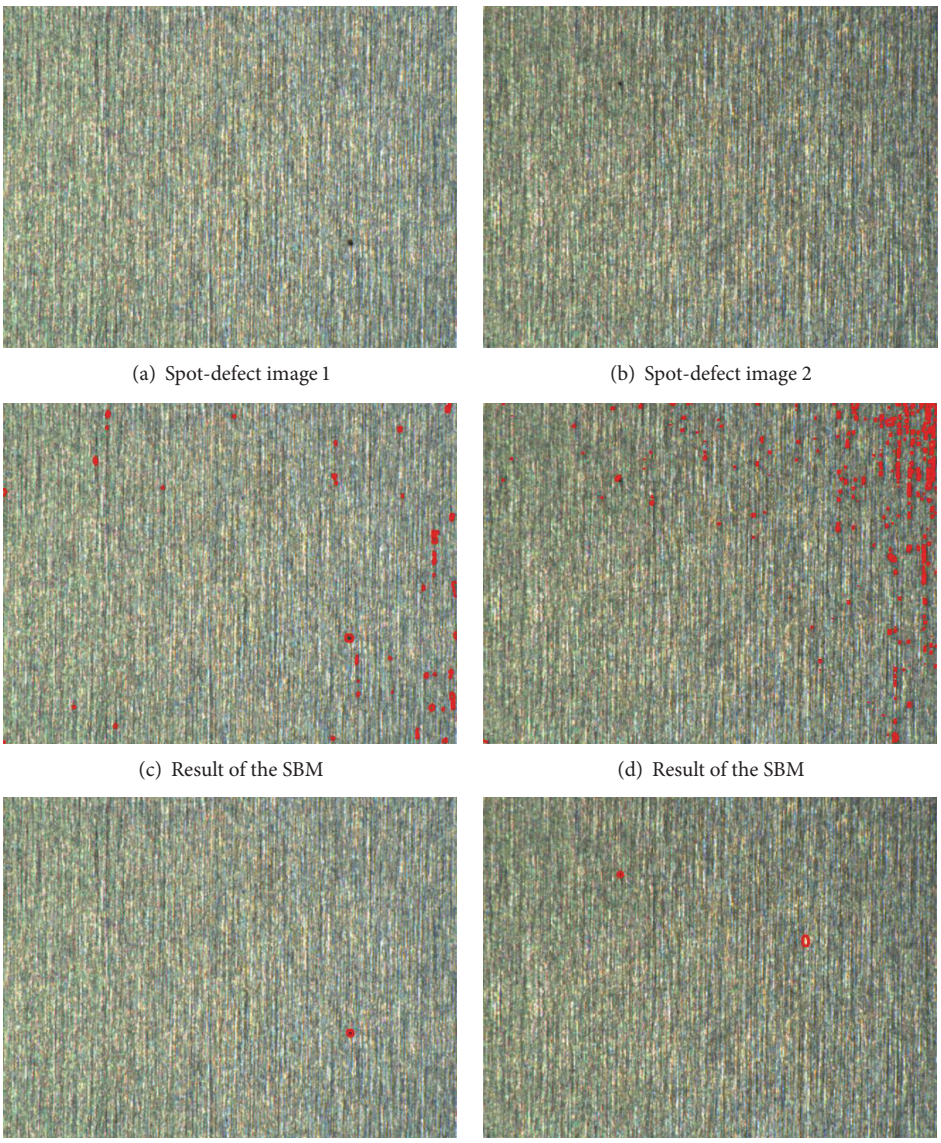

(a) Spot-defect image 1 (b) Spot-defect image 2

(c) Result of the SBM (d) Result of the SBM

(e) Result of the proposed SCACM (f) Result of the proposed SCACM

Figure 6: Results of the different methods for spot-defect image 1 and image 2.

Therefore, the LSM formulation of (4) is as follows:

$$\min_{\phi} E(m_1, m_2, \phi) = \int |\nabla H(\phi)| + \lambda \cdot \int |S(x) - m_1|^2 H(\phi)\, dx + \lambda \cdot \int |S(x) - m_2|^2 (1 - H(\phi))\, dx, \tag{7}$$

where ϕ is level set function and $H(\phi)$ is Heaviside function.

Although the LSM is a successful numerical method to solve (4), the level set minimization problem of (7) is a nonconvex energy minimization problem. This means that the final solution depends on the initial contour. In other words, a bad initial position can lead to a bad solution. It should be noted that the great watershed in optimization is not between linearity and nonlinearity but between convexity and nonconvexity. In order to find exact global solutions of geometric nonconvex problems, Bresson et al. [14] presented a convex relaxation technique. Recently, Brown et al. [15] proposed completely convex formulation of the Chan-Vese model. Inspired by these methods mentioned above, a new convex active contour model based saliency is proposed. Equation (7) is firstly reformulated as follows:

$$\min_{\phi \in \{0,1\}} E(m_1, m_2, \phi) = \int |\nabla \phi| + \lambda \cdot \int |S(x) - m_1|^2 \phi\, dx + \lambda \cdot \int |S(x) - m_2|^2 (1 - \phi)\, dx. \tag{8}$$

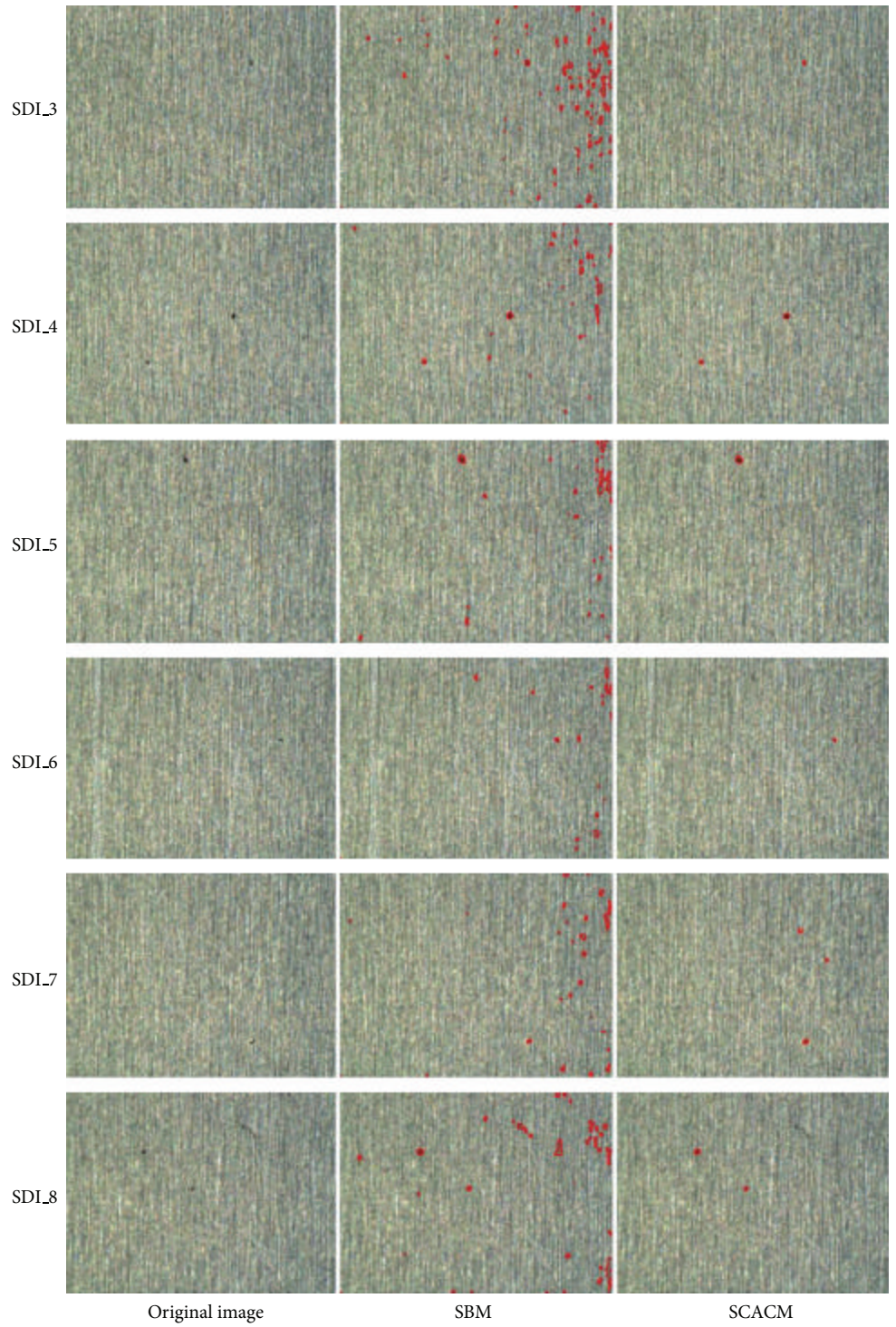

Figure 7: Results of the different methods for spot-defect images (SDI_3~SDI_8).

In order to avoid any confusion with the LSM, the notation ϕ is changed into u. Function u is constrained in $[0, 1]$. Equation (8) is reformulated as follows:

$$\min_{u\in[0,1]} E(m_1, m_2, u) = \int |\nabla u| + \lambda \cdot \int |S(x) - m_1|^2 u \, dx + \lambda \cdot \int |S(x) - m_2|^2 (1 - u) \, dx. \tag{9}$$

Minimizing (9) with respect to u is equivalent to minimizing the saliency convex active contour model (SCACM):

$$\min_{u\in[0,1]} E^{\mathrm{SCACM}}(m_1, m_2, u) = \int |\nabla u| \, dx + \lambda \cdot \int r \cdot u \, dx, \tag{10}$$

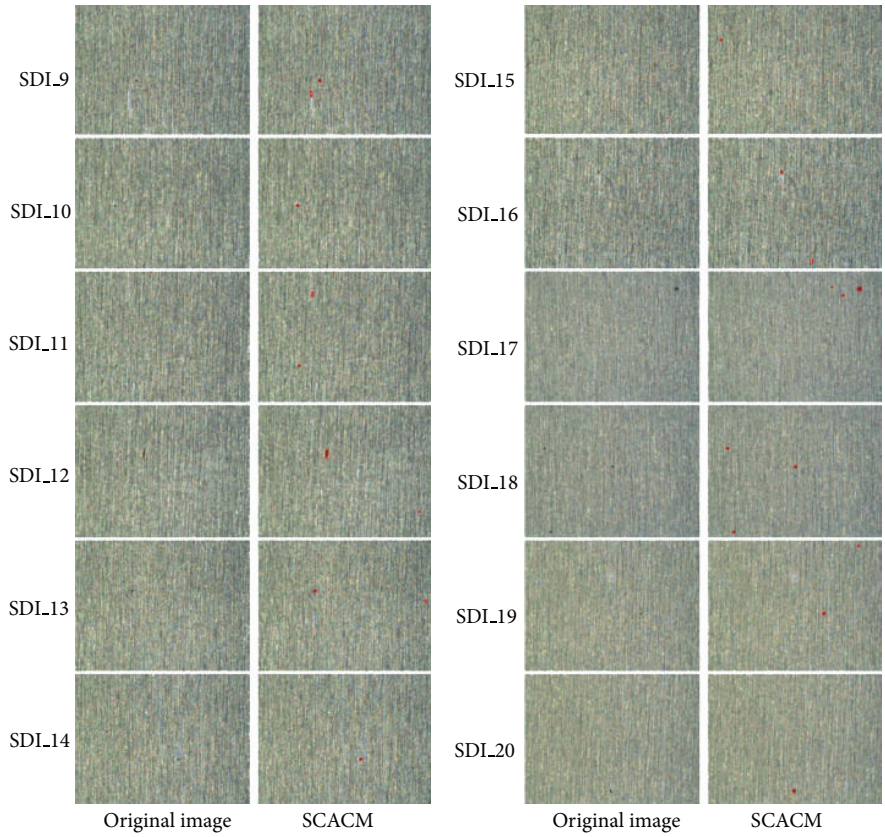

FIGURE 8: Results of the SCACM for spot-defect images (SDI_9~SDI_20).

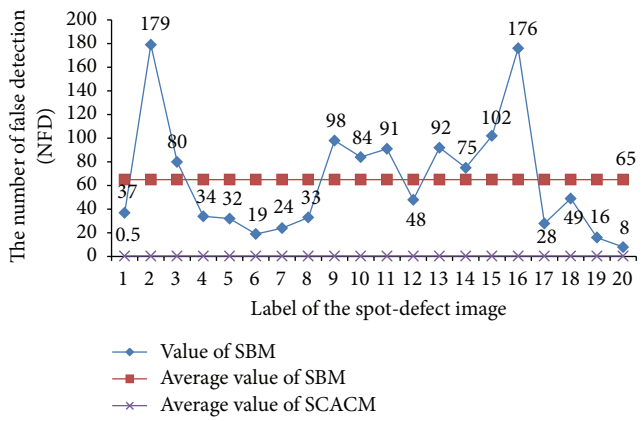

FIGURE 9: The NFD value of the two methods in spot-defect images (SDI_1~SDI_20).

where $\int |\nabla u| \mathrm{d}x$ is the weighted total variation of function u, and r is defined as

$$r = \left|S(x) - m_1\right|^2 - \left|S(x) - m_2\right|^2. \tag{11}$$

In view of the fact that the numerical minimization schemes of LSM are slow to converge to the minimizer, a fast and accurate numerical minimization algorithm for (10) is introduced in this work. This algorithm is named the split Bregman method, which is proposed by Goldstein et al. [16]. A new vector function $\mathbf{d}$ is introduced as follows:

$$\min_{u\in[0,1],\mathbf{d}} E^{\mathrm{SCACM}}(m_1, m_2, u) = \int |\mathbf{d}| + \lambda \cdot r \cdot u \, \mathrm{d}x, \quad \text{such that } \mathbf{d} = \nabla u. \tag{12}$$

The constraint $\mathbf{d} = \nabla u$ is enforced using the efficient Bregman iteration approach [13] defined as

$$\left(u^{k+1}, \mathbf{d}^{k+1}\right) = \min_{u\in[0,1],\vec{\mathbf{d}}} \int |\mathbf{d}| + \lambda \cdot r \cdot u + \frac{\mu}{2}\left|\mathbf{d} - \nabla u - \mathbf{b}^k\right| \mathrm{d}x, \quad k \geq 0,$$

$$\mathbf{b}^{k+1} = \mathbf{b}^k + \nabla u^{k+1} - \mathbf{d}^{k+1}. \tag{13}$$

The minimizing solution u^{k+1} is characterized by the optimality condition:

$$\mu \Delta u = \lambda \cdot r + \mu \cdot \mathrm{div}\left(\mathbf{d}^k - \mathbf{b}^k\right), \quad u \in [0,1]. \tag{14}$$

A fast approximated solution is provided by a Gauss-Seidel iterative scheme; that is, for $n \geq 0$,

$$\alpha_{i,j} = \mathbf{d}_{i-1,j}^{x,k} - \mathbf{d}_{i,j}^{x,k} - \mathbf{b}_{i-1,j}^{x,k} + \mathbf{b}_{i,j}^{x,k} + \mathbf{d}_{i,j-1}^{y,k} - \mathbf{d}_{i,j}^{y,k} - \mathbf{b}_{i,j-1}^{y,k} + \mathbf{b}_{i,j}^{y,k},$$

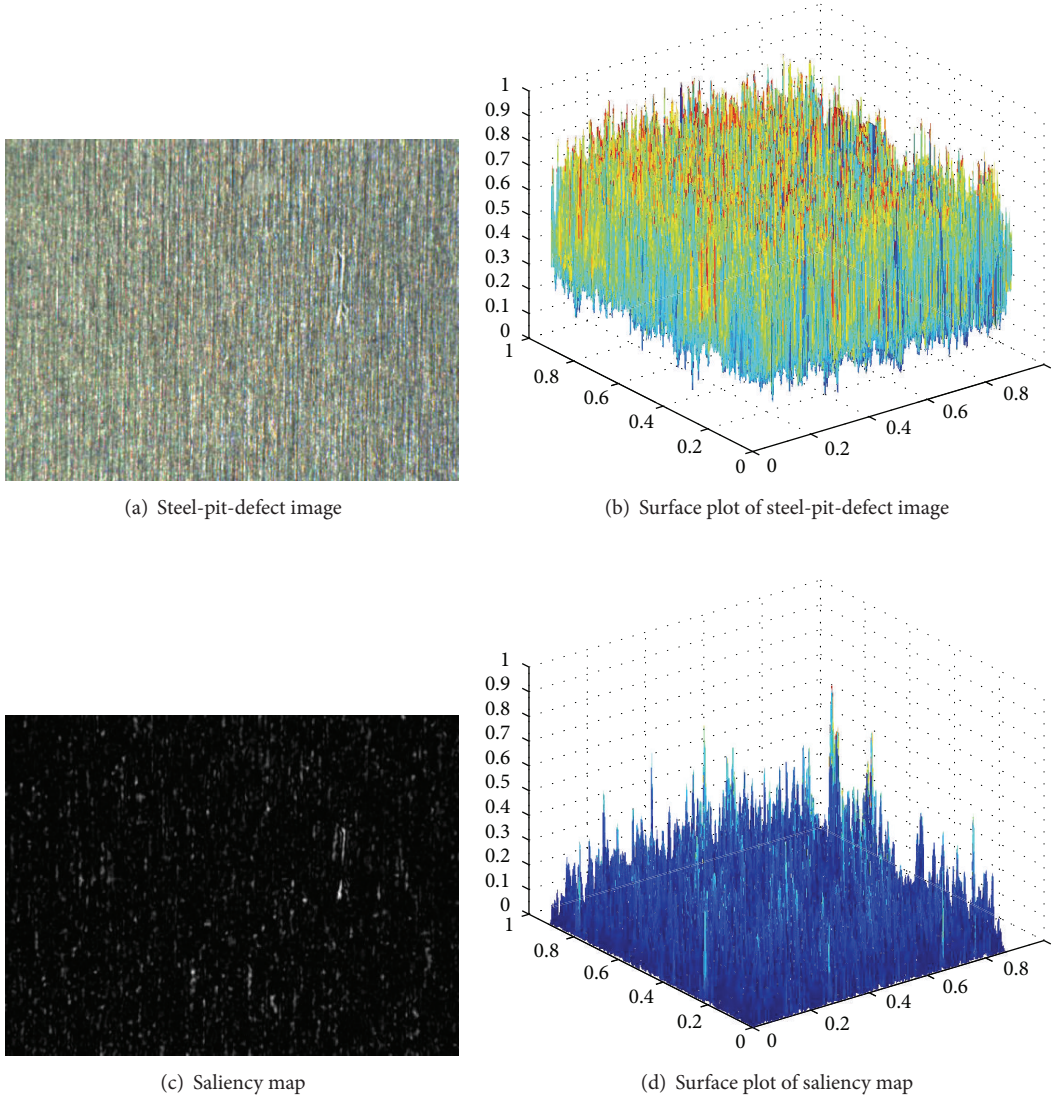

(a) Steel-pit-defect image

(b) Surface plot of steel-pit-defect image

(c) Saliency map

(d) Surface plot of saliency map

FIGURE 10: Saliency map and surface plot of the steel-pit-defect image.

$$\beta_{i,j} = \frac{1}{4}\left(u_{i-1,j}^{k,n} + u_{i+1,j}^{k,n} + u_{i,j-1}^{k,n} + u_{i,j+1}^{k,n} - \frac{\lambda}{\mu}r + \alpha_{i,j}\right),$$
$$u_{i,j}^{k+1,n+1} = \max\left\{\min\left\{\beta_{i,j}, 1\right\}, 0\right\}. \tag{15}$$

The minimizing solution $\mathbf{d}^{k+1}$ is given by soft threshold:

$$\mathbf{d}^{k+1} = \frac{\nabla u^{k+1} + \mathbf{b}^k}{\left|\nabla u^{k+1} + \mathbf{b}^k\right|} \max\left(\left|\nabla u^{k+1} + \mathbf{b}^k\right| - \mu^{-1}, 0\right). \tag{16}$$

The main steps of the proposed SCACM scheme for detecting micro surface defects in textured background images can be summarized as follows.

Step 1. Calculate the saliency map for the input defect image according to the method described in Section 3.1 (Figure 4).

Step 2. Initialize the local Gaussian window $W_k(x)$. The standard deviation σ is set as 3, and the size of the window is determined as $(4\sigma + 1) \times (4\sigma + 1)$.

Step 3. Calculate the initial values m_1^k and m_2^k for m_1 and m_2 using (5) and (6), respectively. Meanwhile, calculate the initial values r^k for r using (11).

Step 4. Initialize the basic parameters of the Gauss-Seidel iterative scheme. Meanwhile, solve (3.2) to obtain u^{k+1}.

Step 5. Solve (16) to obtain $\mathbf{d}^{k+1}$. Then, solve (13) to obtain $\mathbf{b}^{k+1}$.

Step 6. If the inequality $\|u^{k+1} - u^k\| > \varepsilon$ is true, then end. If not, consider $n = n + 1$ and update the values m_1^{k+1} and m_2^{k+1}, and then repeat the algorithm from Step 3.

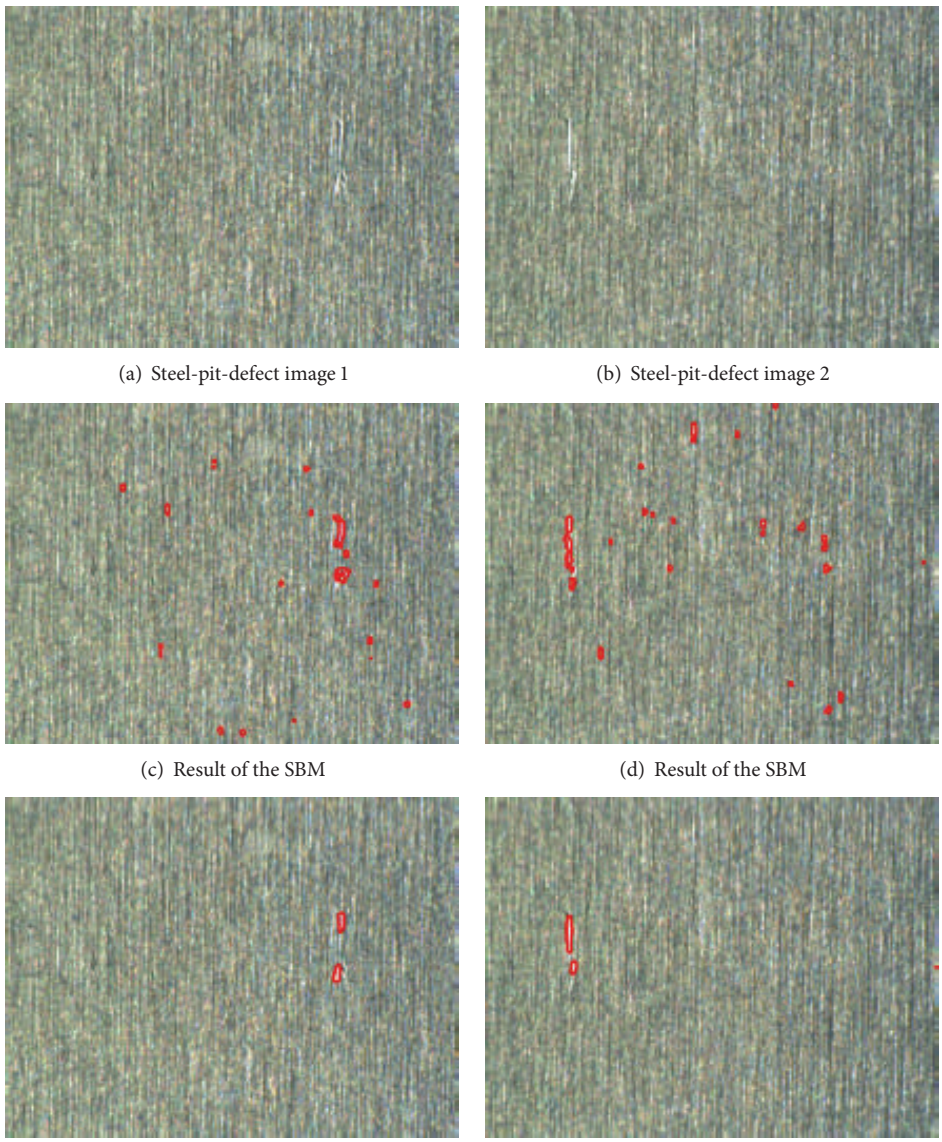

(a) Steel-pit-defect image 1 (b) Steel-pit-defect image 2

(c) Result of the SBM (d) Result of the SBM

(e) Result of the proposed SCACM (f) Result of the proposed SCACM

Figure 11: Results of the different methods for steel-pit-defect image 1 and image 2.

Step 7. Check the final edges of curves; if the edges are nonnull (i.e., existing defects), then they are displayed on the input image. Otherwise, the input image does not have any defects (i.e., the image can be deleted).

4. Experimental Results and Discussion

In this section, we evaluate the performance of the proposed method for detecting micro surface defects including spot-defect and steel-pit-defect. Meanwhile, the proposed method is compared with another method on the detection of micro surface defects.

4.1. Implementation Details. The important basic parameters of the proposed method are set as follows: the size of the Gaussian blur window in Section 3.1 is set as 5×5; the standard deviation σ of local Gaussian window in Section 3.2 is set as 3; λ and μ are set as 10 and 1000, respectively. Moreover, the split Bregman method (SBM), which is proposed by Goldstein et al. [16], is compared with the proposed method for detecting micro surface defects. The performance of these methods mentioned above is evaluated by the following performance criteria: the number of true detection (NTD), the number of false detection (NFD), and the number of missed detection (NMD). Furthermore, the code of these methods is run in Matlab 7.10 (R2010a) software on Pentium (R) Dual-Core machine with 2.8 GHz and 4 GB of memory and the Windows XP operating system. The demo code of the proposed SCACM can be downloaded from our homepage: http://faculty.neu.edu.cn/yunhyan/SCACM.html.

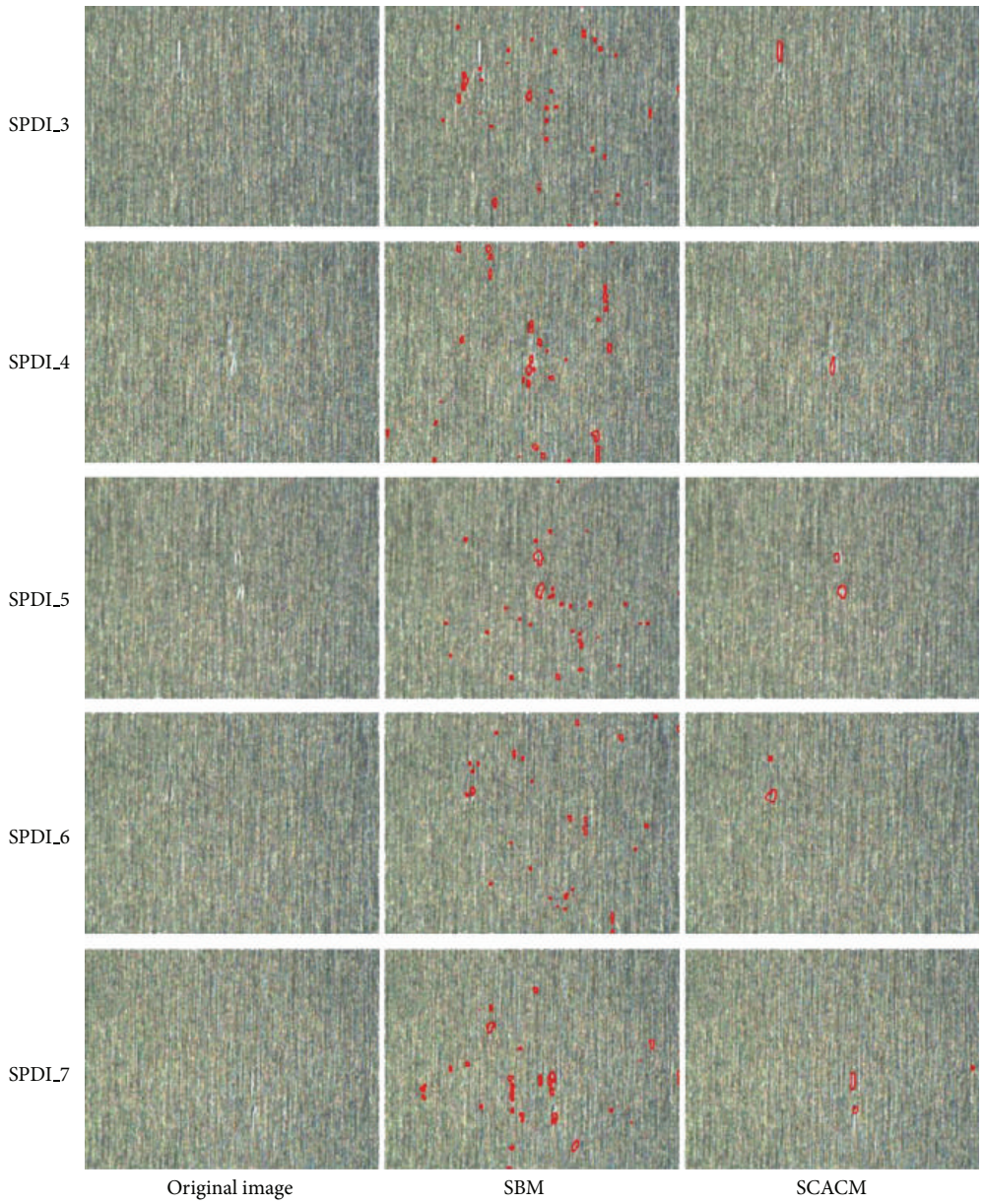

Figure 12: Results of the different methods for steel-pit-defect images (SPDI_3~SPDI_7).

4.2. Spot-Defect Detection. Spot-defect is one of the most common defect types in micro surface defect of silicon steel strip. Therefore, we firstly evaluate the performance of the SBM and the proposed SCACM for detecting spot-defect. Figure 6 illustrates the experimental results for the two methods in spot-defect image 1 and image 2. As is shown in Figures 6(c) and 6(d), although the SBM can detect the micro surface defects in the cluttered background, SBM increases the number of false detection. On the contrary, in Figures 6(e) and 6(f), the proposed SCACM not only detects all of the micro surface defects but also reduces the number of false detection.

To further evaluate the performance of the two methods in spot-defect images, another eighteen spot-defect images are employed to evaluate the performance of the method. Here, the spot-defect image is abbreviated as SDI; for instance, spot-defect image 3 is abbreviated as SDI_3. Figure 7 shows the experimental results for the two methods in spot-defect image 3 to image 8 (SDI_3~SDI_8). Obviously, it is observed that SBM detects too many false objects due to the clutter background. Although the proposed SCACM detects two false objects in SDI_7, it detects almost all of the microdefects without any false objects.

Table 1 shows the performance criteria of detecting spot-defect (SDI_1~SDI_8) for the two methods in detail. As it could be seen in Table 1, the two methods almost have the same number of true detection (NTD), while the NFD value of SBM is far greater than the one of SCACM. Moreover, except in the SDI_8, the two methods do not have the number of missed detection.

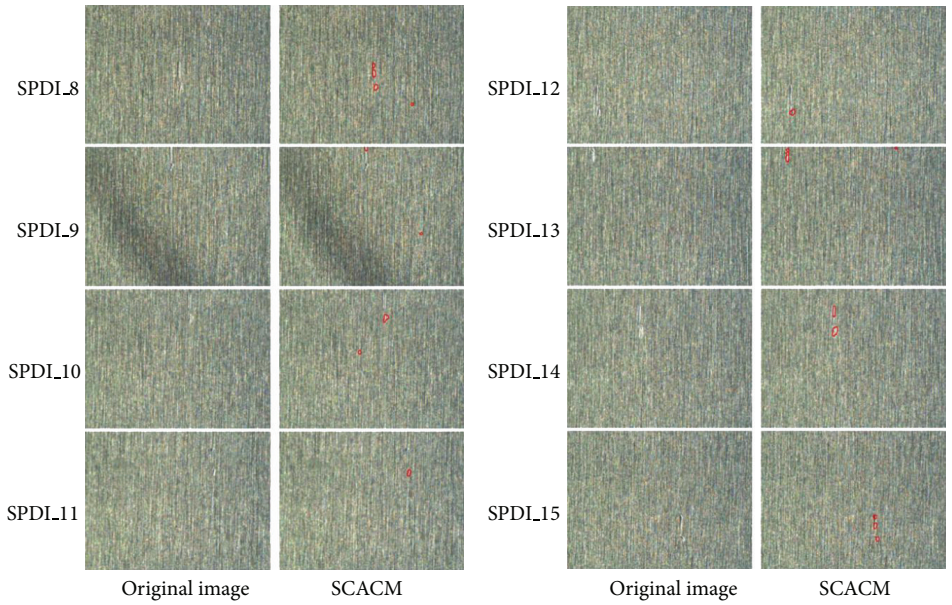

Figure 13: Results of the different methods for steel-pit-defect images (SPDI_8~SPDI_15).

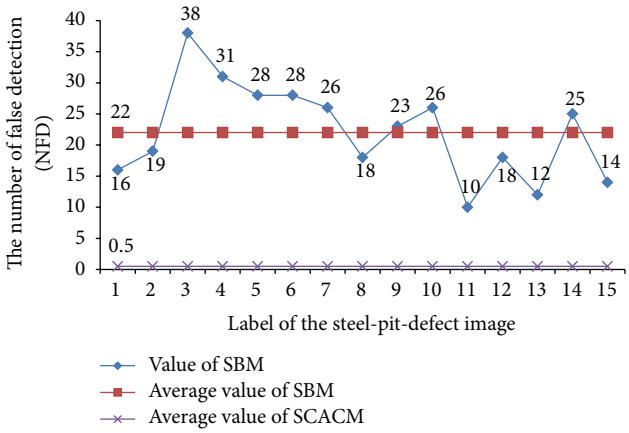

Figure 14: The NFD value of the two methods in steel-pit-defect images (SPDI_1~SPDI_15).

Due to the fact that the SCACM presented better experimental performance than that of SBM, Figure 8 only shows the experimental results for SCACM in spot-defect image 9 to image 20 (SDI_9~SDI_20). In addition, Figure 9 illustrates the NFD value of the two methods in spot-defect images (SDI_1~SDI_20). As is shown in Figure 9, the NFD average value of SBM is 65, while the NFD average value of SCACM is only 0.5. Therefore, Figures 8 and 9 further confirmed the performance of the proposed SCACM for detecting spot-defect.

4.3. Steel-Pit-Defect Detection. Steel-pit-defect is another common defect type in micro surface defect of silicon steel strip. Different from the spot-defect, the shape of the steel-pit-defect is like that of a strip line and the intensity of the steel-pit-defect is more bright. Figure 10 presents the saliency map and surface plot of the steel-pit-defect image. As it could be seen in Figure 10(c), the cluttered background is suppressed in the saliency map. Furthermore, as it could be seen in Figures 10(b) and 10(d), the difference between the interesting steel-pit-defect object and the cluttered background is amplified.

Figure 11 shows the experimental results for the two methods in steel-pit-defect image 1 and image 2. From Figures 11(c) and 11(d), it is observed that SBM detects a larger number of false detection in the cluttered background. However, in Figures 11(e) and 11(f), the proposed SCACM detects all of the micro surface defects without any false detection.

Table 1: The performance criteria of detecting spot-defect for two methods.

Image	Method	NTD	NFD	NMD
SDI_1	SBM	1	37	0
	SCACM	1	0	0
SDI_2	SBM	1	179	0
	SCACM	1	1	0
SDI_3	SBM	1	80	0
	SCACM	1	0	0
SDI_4	SBM	2	34	0
	SCACM	2	0	0
SDI_5	SBM	1	32	0
	SCACM	1	0	0
SDI_6	SBM	1	19	0
	SCACM	1	0	0
SDI_7	SBM	1	24	0
	SCACM	1	2	0
SDI_8	SBM	3	33	0
	SCACM	2	0	1

Table 2: The performance criteria of detecting steel-pit-defect for two methods.

Image	Method	NTD	NFD	NMD
SPDI_1	SBM	2	16	0
	SCACM	2	0	0
SPDI_2	SBM	2	19	0
	SCACM	2	0	0
SPDI_3	SBM	0	38	1
	SCACM	1	0	0
SPDI_4	SBM	1	31	0
	SCACM	1	0	0
SPDI_5	SBM	2	28	0
	SCACM	2	0	0
SPDI_6	SBM	2	28	0
	SCACM	2	0	0
SPDI_7	SBM	1	26	1
	SCACM	2	1	0

In addition, to further evaluate the performance of the two methods in steel-pit-defect images, another thirteen steel-pit-defect images are employed to evaluate the performance of the method. In this work, the steel-pit-defect image is abbreviated as SPDI; for instance, steel-pit-defect image 3 is abbreviated as SPDI_3. Figure 12 illustrates the experimental results for the two methods in steel-pit-defect image 3 to image 7 (SPDI_3~SPDI_7). Due to the clutter background, SBM detects too many false objects. However, except that the SPDI_7 has a false object, the proposed SCACM detects almost all of the microdefects without any false objects. Table 2 shows the performance criteria of detecting steel-pit-defect (SPDI_1~SPDI_7) for the two methods in detail. As expected, the two methods almost have the same NTD value, while the NFD value of SBM is far greater than the one of SCACM. Moreover, the NMD value of SBM is 1 in SPDI_3 and SPDI_7, respectively, while the SCACM does not have any missed detection.

Similar to Section 4.2, Figure 13 only shows the experimental results for SCACM in steel-pit-defect image 8 to image 15 (SPDI_8~SPDI_15). Furthermore, Figure 14 illustrates the NFD value of the two methods in steel-pit-defect images (SPDI_1~SPDI_15). As is shown in Figure 14, the NFD average value of SBM is 22, while the NFD average value of SCACM is only 0.5. As expected, Figures 13 and 14 further confirmed the performance of the proposed SCACM for detecting steel-pit-defect.

4.4. Discussion. On the whole, the proposed SCACM presents good performance for detecting micro surface defects including spot-defect and steel-pit-defect. Even in the cluttered background, the SCACM detected almost all of the microdefects without any false objects. In addition, we also investigated a different size of the Gaussian blur window, which was set as 3×3. As expected, the 3×3 window obtained the same experiment results as those of the 5×5 window. Therefore, the Gaussian blur window can also be set as 3×3 in this work.

5. Conclusion

In this research, a new detection method based on the saliency convex active contour model is presented to detect the micro surface defect of silicon steel strip. In order to highlight the potential objects, the visual saliency extraction is employed to suppress the clutter background in the proposed method. The extracted saliency map is then exploited as a feature, which is fused into a convex energy minimization function of local-based active contour. The split Bregman numerical minimization algorithm is introduced to separate the micro surface defects from cluttered background. Moreover, two typical micro surface defects of silicon steel strip, that is, spot-defect and steel-pit-defect, are used to evaluate the performance of the proposed method. Experimental results demonstrate that the proposed method presents good performance for detecting micro surface defects. The proposed method detects almost all of the microdefects without any false objects even in the cluttered background.

Future perspectives of this work include extension of defect type and classification of the micro surface defect.

Acknowledgments

This work is supported by the National Natural Science Foundation of China (51374063) and the Fundamental Research Funds for the Central Universities (N120603003).

References

[1] C. Eitzinger, W. Heidl, E. Lughofer et al., "Assessment of the influence of adaptive components in trainable surface inspection systems," *Machine Vision and Applications*, vol. 21, no. 5, pp. 613–626, 2010.

[2] E. Lughofer, J. E. Smith, M. A. Tahir et al., "Human-machine interaction issues in quality control based on online image classification," *IEEE Transactions on Systems, Man, and Cybernetics A*, vol. 39, no. 5, pp. 960–971, 2009.

[3] K. C. Song and Y. Y. Yan, "A noise robust method based on completed local binary patterns for hot-rolled steel strip surface defects," *Applied Surface Science*, vol. 285, pp. 858–864, 2013.

[4] P. Caleb-Solly and J. E. Smith, "Adaptive surface inspection via interactive evolution," *Image and Vision Computing*, vol. 25, no. 7, pp. 1058–1072, 2007.

[5] J. Li, J. Shi, and T.-S. Chang, "On-line seam detection in rolling processes using snake projection and discrete wavelet transform," *Journal of Manufacturing Science and Engineering*, vol. 129, no. 5, pp. 926–933, 2007.

[6] E. Pan, L. Ye, J. Shi, and T.-S. Chang, "On-line bleeds detection in continuous casting processes using engineering-driven rule-based algorithm," *Journal of Manufacturing Science and Engineering*, vol. 131, no. 6, pp. 0610081–0610089, 2009.

[7] J. P. Yun, S. Choi, and S. W. Kim, "Vision-based defect detection of scale-covered steel billet surfaces," *Optical Engineering*, vol. 48, no. 3, Article ID 037205, 2009.

[8] J. P. Yun, S. Choi, J.-W. Kim, and S. W. Kim, "Automatic detection of cracks in raw steel block using Gabor filter optimized by

univariate dynamic encoding algorithm for searches (uDEAS)," *NDT and E International*, vol. 42, no. 5, pp. 389–397, 2009.

[9] F. G. Bulnes, R. Usamentiaga, D. F. García, and J. Molleda, "Vision-based sensor for early detection of periodical defects in web materials," *Sensors*, vol. 12, no. 8, pp. 10788–10809, 2012.

[10] A. Landström and M. J. Thurley, "Morphology-based crack detection for steel slabs," *IEEE Journal of Selected Topics in Signal Processing*, vol. 6, pp. 866–875, 2012.

[11] X. W. Zhang, W. Li, J. Xi, Z. Zhang, and X. N. Fan, "Surface defect target identification on copper strip based on adaptive genetic algorithm and feature saliency," *Mathematical Problems in Engineering*, vol. 2013, Article ID 504895, 10 pages, 2013.

[12] R. Achanta, S. Hemami, F. Estrada, and S. Susstrunk, "Frequency-tuned salient region detection," in *Proceedings of the the 27th IEEE Conference on Computer Vision and Pattern Recognition (CVPR '09)*, pp. 1597–1604, Miami, Fla, USA, 2009.

[13] R. Achanta and S. Süsstrunk, "Saliency detection using maximum symmetric surround," in *Proceedings of the 17th IEEE International Conference on Image Processing (ICIP '10)*, pp. 2653–2656, Hong Kong, China, September 2010.

[14] X. Bresson, S. Esedoğlu, P. Vandergheynst, J.-P. Thiran, and S. Osher, "Fast global minimization of the active contour/snake model," *Journal of Mathematical Imaging and Vision*, vol. 28, no. 2, pp. 151–167, 2007.

[15] E. S. Brown, T. F. Chan, and X. Bresson, "Completely convex formulation of the Chan-Vese image segmentation model," *International Journal of Computer Vision*, vol. 98, no. 1, pp. 103–121, 2012.

[16] T. Goldstein, X. Bresson, and S. Osher, "Geometric applications of the split Bregman method: segmentation and surface reconstruction," *Journal of Scientific Computing*, vol. 45, no. 1-3, pp. 272–293, 2010.